

---

# The Meeseeks Mesh: Spatially Consistent 3D Adversarial Objects for BEV Detector

---

Aixuan Li, Mochu Xiang, Jing Zhang, Yuchao Dai✉  
Northwestern Polytechnical University, China  
✉ Corresponding author: daiyuchao@nwpu.edu.cn

## Abstract

3D object detection is a critical component in autonomous driving systems. It allows real-time recognition and detection of vehicles, pedestrians and obstacles under varying environmental conditions. Among existing methods, 3D object detection in the Bird’s Eye View (BEV) has emerged as the mainstream framework. To guarantee a safe, robust and trustworthy 3D object detection, 3D adversarial attacks are investigated, where attacks are placed in 3D environments to evaluate the model performance, *e.g.* putting a film on a car, clothing a pedestrian. The vulnerability of 3D object detection models to 3D adversarial attacks serves as an important indicator to evaluate the robustness of the model against perturbations. To investigate this vulnerability, we generate **non-invasive 3D adversarial objects** tailored for real-world attack scenarios. Our method verifies the existence of **universal adversarial objects** that are spatially consistent across time and camera views. Specifically, we employ differentiable rendering techniques to accurately model the spatial relationship between adversarial objects and the target vehicle. Furthermore, we introduce an **occlusion-aware module** to enhance visual consistency and realism under different viewpoints. To maintain attack effectiveness across multiple frames, we design a **BEV spatial feature-guided optimization strategy**. Experimental results demonstrate that our approach can reliably suppress vehicle predictions from state-of-the-art 3D object detectors, serving as an important tool to test robustness of 3D object detection models before deployment. Moreover, the generated adversarial objects exhibit strong generalization capabilities, retaining its effectiveness at various positions and distances in the scene.

## 1 Introduction

3D object detection [1, 2] has been widely used in autonomous drivings. Compared to Lidar-based solutions [3, 4, 5], pure vision solutions [6, 7] have received attention due to their low cost. Among those vision solutions, 3D object detection models that utilize multi-view image features to construct bird’s eye view (BEV) features have emerged as the mainstream frameworks, which are proven to be superior in improving the understanding of the scene and the detection performance [8, 9, 10].

As autonomous driving is especially safety-critical [11, 12, 13, 14], ensuring the robustness and reliability of the perception systems is of paramount importance. Despite their remarkable high accuracy, these methods remain vulnerable to delicately crafted adversarial perturbations that can mislead model predictions. In autonomous driving scenarios, such attacks can cause false 3D bounding boxes [15, 16] or the complete disappearance of an object [17, 18, 11] in the BEV view, potentially leading to hazardous outcomes such as collisions or abrupt emergency braking.

Motivated by these risks, some adversarial approaches are proposed to investigate the robustness of 3D object detection models. In particular, these approaches target single-image-oriented vehicle detection models, *i.e.* camouflaged attack [19, 20, 21, 22], but show incapacity to achieve effective

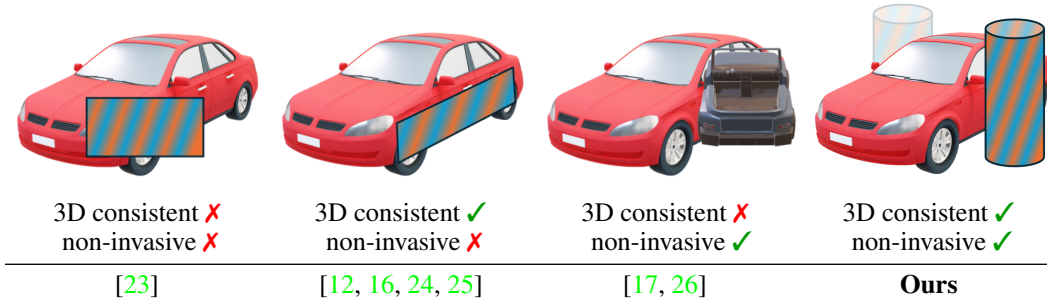


Figure 1: **Comparison of different adversarial attacks for 3D object detection** with respect to 3D consistency and non-invasiveness.

adversarial attacks for BEV models [6, 5, 7], which are more widely adopted in autonomous systems. The combination of multiple perspectives in BEV models provides a holistic representation of the current scene, while being more suitable for sensing the surrounding situation and making predictions. Thus, the robustness of 3D object detection in BEV deserves extensive investigation. We aim to expose potential vulnerabilities in autonomous systems that employ BEV as a central representation to support the development of safer and more reliable autonomous vehicles.

Existing adversarial approaches for 3D object detection in BEV typically suffer from two limitations: invasiveness and 3D inconsistency (see Fig. 1). First, these attacks often modify the texture or physical structure of the target object, *e.g.*, through adversarial textures [23] or geometry [27, 12], resulting in invasive interventions. While conceptually simple, such methods lack scalability; it is impractical to alter every vehicle or expect pedestrians to wear specially designed adversarial garments, especially when aiming for broad and unpredictable impact. Second, some attacks operate in the image space using flat 2D perturbations [16, 24], which overlook the 3D structure of objects. As a result, they fail to maintain effectiveness across varying viewpoints and lighting conditions, limiting their realism and robustness in real-world 3D perception systems.

We depart from existing methods by proposing a novel contactless 3D adversarial attack, **Meeseeks Mesh**, whose sole purpose is to attack and disrupt multi-view autonomous driving models. We investigate a security vulnerability in BEV modeling: the existence of a universal adversarial object that, when placed near a vehicle without direct contact, can mislead the model’s predictions and cause harmful outcomes. Unlike prior methods, our approach does not require physical modification of the target. Instead, we introduce and optimize a 3D adversarial object strategically placed in the scene to alter the perception of nearby targets. By leveraging geometric consistency across views, our method presents a more realistic and potent threat to BEV-based autonomous driving systems.

## 2 Related Works

### 2.1 3D Adversarial Attack

3D adversarial attack is to intentionally manipulate 3D input data [28, 29, 30, 31] in order to fool a 3D machine learning system into making incorrect predictions, where the system can be typically a detection system or a recognition system. Early foundational work by [31] provided the first evidence of physically realizable 3D adversarial objects for classification, showing their effectiveness in white-box settings under controlled transformations. Instead of generating perturbation in the image space, [28] achieved white-box attacks by altering the texture of 3D objects using rendered image supervision, highlighting the vulnerability of models to texture-based manipulations in the context of object classification and visual question answering. Similarly, [29] demonstrated that modifying either the texture or vertex positions of mesh objects with adversarial 3D meshes can fool 2D vision tasks, *e.g.*, 2D object classification and detection. [20] improved the stealthiness of 3D texture attacks with visually natural physical adversarial camouflages, and applied the generated perturbation to 2D vision tasks. Different to [20] that only generated a camouflage patch for adversarial attack, [19] designed full-coverage, high-resolution adversarial textures for vehicles using multi-view datasets, significantly improving camouflage attacks in long-range, multi-view detection scenarios. Following

the adversarial camouflage setting, [21] used neural renderers to simulate real-world transformations, generating more plausible and effective camouflage textures for 2D vehicle detection tasks. [32] generated optimized printable adversarial stickers from a 3D model to test robustness of a 2D classification model. [22] introduced geometry-independent adversarial textures for adversarial camouflage to conceal any 3D vehicle from 2D detectors using triplanar mapping, making the attacks transferable to different vehicle types without the need of shape-specific adjustments. [33] proposed a transferable **targeted** attack strategy for 2D classification by perturbing 3D meshes reconstructed from real-world multi-view images. In contrast to prior approaches, our method targets realistically deployable, non-invasive attacks with broader impact. Rather than manipulating the prediction of the adversarial object itself, we design the adversarial object to disrupt the model’s perception of other targets, even when there is no physical contact with them.

## 2.2 Non-invasive Adversarial Attack

As discussed above, adversarial camouflage is one of the mainstream of 3D adversarial attack, which typically adds physically realizable textures or patterns to objects, making it invasive attack. Non-invasive adversarial attacks do not require modification of the target object, which leave no permanent trace, making them harder to detect or prove post-event. One of the earliest works [34] utilized data augmentation with geometric transformations to make the generated patch perturbations effective even after covering the image with different transformations. Expanding on this idea, [35] verified the possibility of attacking human detection models when the perturbed region is not located on the human body. [36] introduced an innovative method that utilizes image generators to craft perturbations in the latent space of category features, allowing the construction of robust adversarial regions. For optical attack, [37] proposed a stealthy attack using geometric shapes made up of different colored reflected light. Meanwhile, [17] generated a 3D vehicle to attack 3D object detection in a driving scene. The attacking vehicle, represented by NeRF, is rendered from a specific viewpoint and pasted onto the original image to generate a perturbation. Different from the above methods, this paper proposes the first non-invasive 3D adversarial attack method that conforms to the 3D view of the scene and constructs an association between the real scene and the adversarial object.

## 2.3 Adversarial Attack on 3D Object Detection

Adversarial attacks against 3D object detection can be broadly categorized into three main categories: **LiDAR-based attacks** [18, 11, 38, 39, 40] focused on modifying the spatial distribution or quantity of 3D point clouds captured by LiDAR sensors to deceive perception modules. **Camera-LiDAR fusion attacks** [27, 12] typically relied on [41] setups, such as placing adversarial meshes on vehicles [41]. For instance, [27] optimized both the geometry and texture of a mesh to simultaneously attack LiDAR and the 2D camera-based module in a cascaded multi-modal detection pipeline. Similarly, [12] placed a mesh on the roof of a vehicle to achieve stealth. These methods are limited to single-view cameras and introduce a high degree of spatial overlap between the mesh and the vehicle, which alters the vehicle’s geometry and compromises its identity—resulting in what the authors describe as overly relaxed definitions of adversarial targets. Despite these limitations, both studies highlight that RGB-based attacks are more computationally efficient and easier to implement compared to point cloud-based attacks, which inspired our focus on purely visual adversarial attacks.

In the domain of **pure camera-based attacks** [23, 15, 16, 24, 26], several works have evaluated vulnerabilities at the pixel and patch levels [26, 23, 24]. [23] showed that methods without depth estimation and those using multi-frame inputs are more robust against such perturbations. Additionally, both [23] and [24] found that using BEV representations improves overall resistance to adversarial interference. Among recent contributions, [15] optimized a generic poster texture placed on the ground, visible to front and rear cameras, to induce false-positive object detection in BEV-based vision systems. [16] explored a broader approach, inducing large-scale hallucinated objects by pasting adversarial patches both on vehicles and vertically in the scene. In addition, Adv3D [17] employs a NeRF-based renderer [42] to synthesize adversarial vehicles. It inserts two fictitious cars into the scene to erase target objects in the BEV representation. However, the method suffers from inaccurate occlusion modeling and incorrect perspective consistency.

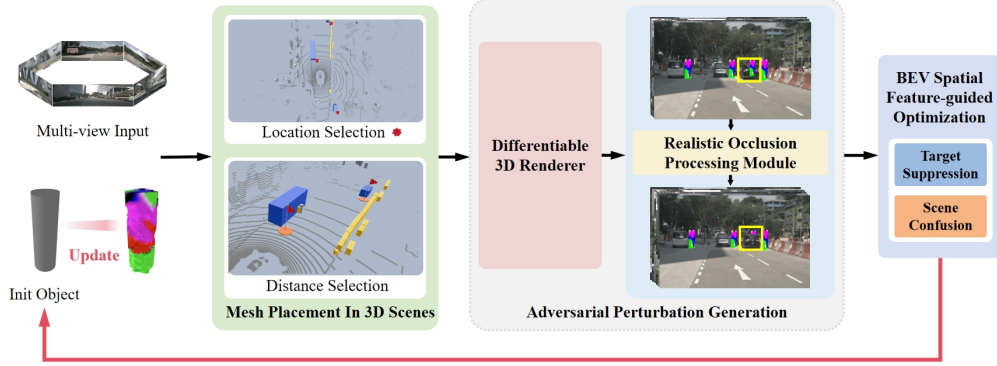


Figure 2: **Overview of our adversarial object generation pipeline.** Appropriate locations are first chosen to place adversarial meshes in the 3D scene (“Mesh Placement in 3D Scene”), which are then rendered onto the input images. Our differentiable renderer ensures 3D-consistent, multi-view renderings with correct perspective. The “Realistic Occlusion Processing Module” further simulates partial visibility for improved robustness. Finally, the adversarial object is optimized via “BEV Spatial Feature-Guided Optimization” to enable effective attacks across both time and space.

### 3 Methodology

#### 3.1 Problem Formulation

The goal of 3D object detection is to localize and classify objects in three dimensions. Specifically, given a set of multi-camera images denoted as  $\mathcal{I} = \{I_1, I_2, \dots, I_N\}$ , where each image  $I_i \in \mathbb{R}^{H \times W \times 3}$  is captured from one of the  $N$  calibrated cameras. The objective is to infer the 3D bounding boxes and semantic categories of all related objects in the scene. Each 3D bounding box is represented as  $B = \{x, y, z, l, w, h, \theta\}$ , where  $(x, y, z)$  denotes the coordinates of the object’s center in the 3D space,  $\{l, w, h\}$  represents the length, width, and height of the bounding box, and  $\theta$  denotes the yaw angle of the object. The corresponding object category is denoted by  $\tau$ .

3D object detection attacks aim to fool the 3D perception systems into misidentifying, mislocalizing or completely missing objects in the 3D environment. In particular, we target 3D object detection in BEV (see Fig. 2) by placing adversarial meshes at strategically chosen locations. Meshes are rendered via a 3D-consistent differentiable renderer with accurate perspective and realistic occlusion, then we optimize the non-invasive mesh to maintain effective attacks across viewpoints and time.

Following the conventional optimization mechanism for 3D object detection [23, 40], we aim to optimize the perturbation by maximizing the model’s prediction error for the target class  $\tau_t$ , *i.e.* vehicles. The objective function for the attack can thus be formulated as:

$$\mathcal{L}_{attack}(\mathcal{I}_{adv}, B_{\tau_t}, f) = \mathcal{L}_{cls}(f(\mathcal{I}_{adv}), \tau_t) + \mathcal{L}_{loc}(f(\mathcal{I}_{adv}), B_{\tau_t}) + \lambda \cdot |\delta|_p, \quad (1)$$

where  $\mathcal{L}_{cls}$  penalizes the model  $f(\cdot)$  for accurately predicting the vehicles, *i.e.* to reduce the confidence score of  $\tau_t$ .  $\mathcal{L}_{loc}$  encourages the model to predict vehicles at incorrect position. The adversarial images  $\mathcal{I}_{adv}$  are constrained with raw images  $\mathcal{I}$  by  $|\delta|_p \leq \epsilon$ , where  $\epsilon$  is the maximum perturbation magnitude allowed and  $p$  is typically 2 or  $\infty$ . Minimizing the attack loss  $\mathcal{L}_{attack}$ , the vehicles will either disappear from the predictions or appear at an incorrect position.

Our main solution consists of the following steps: 1) Automatic selection of suitable regions for adversarial mesh placement (Sec. 3.2). 2) Adversarial multi-view images generation with perspective projection and occlusion-aware simulation (Sec. 3.3). 3) BEV Spatial Feature-Guided Optimization technique (Sec. 3.4). An overview of the proposed pipeline can be found in Fig. 2.

#### 3.2 Mesh Placement in 3D Scenes

We explore whether a unified 3D object can consistently execute multi-frame or multi-view adversarial attacks in realistic 3D scenes for non-contact 3D object detection (see Fig. 2). In contrast to Adv3D [17], which employs NeRF [42] to optimize only vehicle textures (see Fig. 3), our approach

utilizes mesh-based representations, which makes no assumptions about object category, explicitly models perspective occlusions. Furthermore, by adopting mesh representations other than NeRF, we gain direct surface control and improved compatibility with physics-based environments.

A 3D mesh is typically represented as a set of vertices  $\mathcal{V} = \{v_1, v_2, \dots, v_n\} \subset \mathbb{R}^3$ , triangular faces  $\mathcal{F} = \{f_1, f_2, \dots, f_m\}$ , and optional vertex or face textures  $\mathcal{T} = \{t_1, t_2, \dots, t_n\}$ , mapping vertices to 2D texture space. To realistically insert the mesh into a 3D scene, we place it adjacent to vehicles using their 3D bounding boxes  $B$ , ensuring consistent alignment across views. We decompose the placement into two steps, namely location selection and distance to target computation. The former localizes the adversarial object relative to the target vehicle, and the latter refines its 3D coordinates to ensure no physical contact occurs.

**Location Selection:** The mesh is placed near one of the bottom corners of the vehicles’ bounding box to ensure interaction with the detection model. The 8 corners  $\{b_k\}_{k=1}^8$  of the bounding box by offsetting from the center  $(x, y, z)$  along each axis, accounting for orientation  $\theta$ . For example, the coordinates of the right-rear-bottom corner  $b_1$  is  $(x - \frac{l}{2} \cos \theta - \frac{w}{2} \sin \theta, y - \frac{l}{2} \sin \theta + \frac{w}{2} \cos \theta, z - \frac{h}{2})$ . Other corners are defined analogously, with varying combinations of sign on  $\frac{l}{2}, \frac{w}{2}, \frac{h}{2}$ .

To ensure the mesh is tangent but not intersecting with the vehicles, we define the center of the mesh as  $p_m$ . Let  $v_{\vec{n}_{max}}$  denote the maximal distance from the mesh center to any vertex of mesh along direction  $\vec{n}$ . Specifically, when positioning from  $b_1$  with direction  $\vec{n} = -y$ , the center of the mesh is computed as:  $p_m = b_1 + v_{\vec{n}_{max}} \cdot \hat{n}$ , where  $\hat{n}$  is the unit vector in direction  $\vec{n}$ . This ensures that the outermost vertices of the mesh along  $-\hat{n}$  coincide with  $b_1$  when the mesh is in contact.

**Distance to Target:** The distance between the mesh and vehicles  $d$  is defined as the Euclidean distance between the mesh center  $p_m$  and the reference corner  $b_1$ . At  $d = 0$ , the mesh touches the vehicle at  $b_1$ . For  $d > 0$ , the mesh is offset further from  $b_1$  along  $\vec{n}$ :  $p_m = b_1 + (v_{\vec{n}_{max}} + d) \cdot \hat{n}$ . The distance  $d$  is constrained to the range  $(0, d_{max})$ , where  $d_{max}$  ensures the mesh remains relevant to the target vehicle in the scene.

### 3.3 Adversarial Perturbation Generation

After deciding a target region to place the adversarial mesh, the next step is to render it onto the input image for object detection models. Our method ensures 3D consistency by rendering the mesh onto  $N$  calibrated cameras. The mesh is centered at  $p_m = (x_m, y_m, z_m)$  in the vehicle coordinate system, consistent with the current frame’s ego rotation, yielding identity rotation  $R = \mathbf{I}_3$  and translation  $T = p_m^\top$ . Each camera has extrinsics  $(R_i, T_i)$  that map 3D points from the vehicle to the  $i$ -th camera coordinate system. For a mesh vertex  $v_j$  in local coordinates, the transformation is:  $v_j^{\text{cam}_i} = R_i \cdot (R \cdot v_j + T) + T_i$ , where  $v_j^{\text{cam}_i}$  is the  $j$ -th vertex in  $i$ -th camera coordinate frame. This transforms all vertices  $\mathcal{V}$  into the  $i$ -th camera frame coordinate system. We then employ the differentiable renderer PyTorch3D [43] to project 3D vertices to 2D image coordinates via the camera’s intrinsic matrix  $K_i$ . Each vertex  $v_j^{\text{cam}_i}$  is mapped to a 2D point  $(p_{x_j}, p_{y_j})$ , producing an RGB image  $\mathcal{I}_i^{\text{rgb}} \in \mathbb{R}^{H \times W \times 3}$  and a soft mask  $\mathcal{I}_i^{\text{mask}} \in \mathbb{R}^{H \times W \times 1}$  encoding mesh visibility and transparency in the image.

**Realistic Occlusion Processing Module:** To avoid the complexity of full 3D scene reconstruction, we generate adversarial perturbations directly in 2D images, while maintaining consistency with 3D geometry. Occlusions are handled per view using the 3D bounding boxes of annotated objects. For the  $i$ -th view, we project all mesh vertices via  $K_i$  to obtain the mesh’s 2D bounding box  $B_{\text{mesh}}^{2D} = \{x_{\min}, y_{\min}, x_{\max}, y_{\max}\}$ . Similarly, each object’s 3D bounding box  $B_i$  is projected to get  $B_i^{2D}$  through the camera intrinsic and extrinsic matrix. We compute their overlaps:

$$\mathcal{O}(B_{\text{mesh}}^{2D}, B_i^{2D}) = B_{\text{mesh}}^{2D} \cap B_i^{2D}. \quad (2)$$

If  $\mathcal{O} > 0$ , we assess occlusion based on depth. We define the mesh depth as the minimum Euclidean distance between any vertex  $v_j$  of the mesh and the camera center (origin of the camera coordinate):  $d_{\text{mesh}} = \min_j \|v_j\|$ . Similarly, the object depth is the minimum distance from any of its 3D bounding box corners  $b_{k,l}^{\text{cam}_i}$  to the camera, computed as  $d_k = \min_l \|b_{k,l}^{\text{cam}_i}\|$ , where  $k$  indexes the annotated objects in the scene,  $l$  indexes the 8 corners of the 3D bounding box. If  $d_k < b_{\text{mesh}}$ , the object occludes the mesh. To mask occluded regions, we prompt the SAM2 model [44] with  $B_i^{2D}$  to produce a segmentation mask  $M_i^{\text{seg}}$ , which we apply to the mesh mask:  $\mathcal{I}_i^{\text{mask}} \leftarrow \mathcal{I}_i^{\text{mask}} \cdot (1 - M_i^{\text{seg}})$ , which

simulates realistic occlusion under all  $N$  calibration views. Finally, the adversarial image is composed by alpha blending the rendered mesh  $\mathcal{I}_i^{\text{rgb}}$  with the raw background image  $\mathcal{I}_i^{\text{raw}}$ :

$$\mathcal{I}_i^{\text{adv}} = \mathcal{I}_i^{\text{rgb}} \cdot \mathcal{I}_i^{\text{mask}} + (1 - \mathcal{I}_i^{\text{mask}}) \cdot \mathcal{I}_i^{\text{raw}}. \quad (3)$$

### 3.4 BEV Spatial Feature-guided Optimization

Our adversarial attack targets 3D object detection systems by pursuing two primary goals: (1) suppressing correct vehicle predictions within a designated target region, and (2) inducing false predictions in non-target regions to disrupt overall scene understanding. To this end, we optimize the shape and appearance of an adversarial object by minimizing a composite loss function consisting of three components.

**Target Suppression:** To suppress correct predictions within the annotated region, we minimize the sum of heatmap responses in the target area:

$$\mathcal{L}_{\text{cls}} = \sum (f(\mathcal{I}_{\text{adv}})_{\text{heatmap}} * \mathcal{R}_{\tau_t}), \quad (4)$$

where  $\mathcal{R}_{\tau_t}$  denotes the 2D projection of the target 3D bounding box  $B_{\tau_t}$  onto the heatmap space,  $f$  denotes the 3D detection model and  $\mathcal{I}_{\text{adv}}$  is the rendered adversarial multi-camera image set.

Additionally, to disrupt accurate 3D localization, we maximize the discrepancy between the predicted 3D bounding box and the target vehicle ground-truth box  $B$  using an L1 loss:

$$\mathcal{L}_{\text{loc}} = -|f(\mathcal{I}_{\text{adv}})_{\hat{B}} - B_{\tau_t}|, \quad (5)$$

where  $f(\mathcal{I}_{\text{adv}})_{\hat{B}}$  represents the 3D bounding box predicted by the model in the region  $B_{\tau_t}$ .

**Scene Confusion:** To encourage false positives in irrelevant regions, we disturb the global scene representation by minimizing the cosine similarity between BEV features extracted from the adversarial image and the original (unperturbed) image:

$$\mathcal{L}_{\text{sim}} = \cos(f_{\phi}(\mathcal{I}_{\text{adv}}), f_{\phi}(\mathcal{I}_{\text{raw}})) = \frac{f_{\phi}(\mathcal{I}_{\text{adv}}) \cdot f_{\phi}(\mathcal{I}_{\text{raw}})}{\|f_{\phi}(\mathcal{I}_{\text{adv}})\| \times \|f_{\phi}(\mathcal{I}_{\text{raw}})\|}, \quad (6)$$

where  $f_{\phi}(\cdot)$  denotes the BEV feature extractor in model  $f$ , and  $\mathcal{I}_{\text{raw}}$  is the original multi-view image.

The overall objective combines all three components:

$$\min_{\mathcal{V}, \mathcal{T}} \mathcal{L}_{\text{attack}}(\mathcal{V}, \mathcal{T}) = \mathcal{L}_{\text{cls}}(\mathcal{I}_{\text{adv}}(\mathcal{V}, \mathcal{T})) + \alpha \mathcal{L}_{\text{loc}}(\mathcal{I}_{\text{adv}}(\mathcal{V}, \mathcal{T})) + \beta \mathcal{L}_{\text{sim}}(\mathcal{I}_{\text{adv}}(\mathcal{V}, \mathcal{T})), \quad (7)$$

where  $\alpha$  and  $\beta$  are weighting coefficients that balance localization and scene confusion against the classification loss. This formulation ensures the adversarial object (1) prevents correct detection in the target region and (2) induces false detections elsewhere, effectively disrupting the model’s scene-level reasoning. We optimize mesh vertices  $\mathcal{V}$  and textures  $\mathcal{T}$  with Eq. 7 to obtain effective attacks across viewpoints and time.

## 4 Experiments

### 4.1 Experimental setting

**Dataset:** We use the nuScenes dataset [45], a large-scale autonomous driving benchmark with 3D annotations and camera data from six calibrated views. It contains 1,000 scenes collected in Boston and Singapore. Our 3D adversarial perturbations are trained on 28,130 keyframes from the training set and evaluated on 6,019 keyframes from the validation set. Each keyframe provides six images covering the full 360° horizontal field of view.

**Evaluation metrics:** We assess attack effectiveness using the Attack Success Rate (ASR), defined as  $\text{ASR} = 1 - N_{\text{adv}}/N_{\text{init}}$ , where  $N_{\text{adv}}$  and  $N_{\text{init}}$  denote the number of successfully detected vehicles with adversarial and initialized objects, respectively. A detection is considered successful if the predicted bounding box has an Intersection over Union (IoU) above a given threshold with the ground truth, regardless of category correctness. We report ASR across IoU thresholds ranging from 0.2 to 0.7 to account for varying localization strictness. Furthermore, we assess the overall impact of our

Table 1: Performance comparison of BEV-based 3D object detection on adversarial attack.

	Real Occ	Init NDS	Adv NDS	Init mAP	Adv mAP	ASR <sub>0.2</sub>	ASR <sub>0.3</sub>	ASR <sub>0.5</sub>	ASR <sub>0.7</sub>
BEVDet	✗	0.3579	0.2097	0.2625	0.1298	0.594	0.613	0.657	0.715
BEVDet	✓	0.3727	0.2677	0.2797	0.1631	0.425	0.447	0.510	0.550
BEVDet4D	✗	0.4158	0.2762	0.2799	0.1564	0.290	0.321	0.391	0.473
BEVDet4D	✓	0.4304	0.3385	0.2929	0.1885	0.399	0.441	0.508	0.593
BEVFormer	✗	0.4592	0.2876	0.3402	0.1652	0.420	0.463	0.551	0.681
BEVFormer	✓	0.4681	0.3381	0.3565	0.2073	0.260	0.325	0.425	0.559

Table 2: Performance comparison with Adv3d [17]. Ped. means pedestrians.

	Init NDS	Adv NDS	Init mAP	Adv mAP	AP <sub>car</sub>	AP <sub>truck</sub>	AP <sub>Ped.</sub>	AP <sub>barrier</sub>
Ours	0.3579	0.2097	0.2625	0.1298	0.153	0.034	0.287	0.451
Adv3d	0.2820	0.2277	0.1727	0.0967	0.173	0.064	0.240	0.230

adversarial objects on the scene by evaluating the Mean Average Precision (mAP) and the nuScenes Detection Score (NDS) [45].

**Victim Models:** We train non-invasive 3D adversarial objects on three camera-based 3D object detectors: BEVDet [7], BEVDet4D [46], and BEVFormer-small [47]. Both BEVDet and BEVDet4D adopt ResNet-50 as the backbone and utilize class-balanced grouping and sampling [48], with an input image resolution of  $256 \times 704$ . BEVFormer-small uses ResNet-101 as the backbone and operates on images of resolution  $736 \times 1280$ .

**Implementation details:** We keep mesh topology fixed and optimize both vertex positions and texture using Adam (learning rate 0.02), with per-vertex displacement capped at 0.1 units. Unless otherwise noted, the adversarial mesh is placed near the target vehicle’s rear-right-bottom corner. We initialize the mesh as a *cylinder* (radius 0.3, height 2.0), positioned 0.1 units from the target to avoid intersection, the offset is adjusted as the mesh size changes. The mesh location is determined from the current frame and kept fixed across temporal inputs. Training is conducted on eight NVIDIA L40 GPUs for 10 epochs. Due to memory constraints, the number of meshes per image is limited to 4 (BEVDet/BEVDet4D) and 2 (BEVFormer). We set  $\alpha$  and  $\beta$  to 1 in Eq. 7.

## 4.2 Quantitative Results

We present a comparison of white-box attack results on BEVDet, BEVDet4D, and BEVFormer in Tab. 1. Our setup introduces additional objects into the scene, which may occlude the target. "Init" (NDS/mAP) refers to performance with initialized 3D objects, while "Adv" indicates results with adversarial 3D objects. "Real Occ" indicates whether the real occlusion handling module is applied. Across all models, the transition from "Init" to "Adv" demonstrates a clear drop in performance, validating the effectiveness of our temporally and view-consistent attack strategy. Notably, our results confirm that placing an adversarial object near a target is sufficient to disrupt detection. Interestingly, BEVDet4D shows strong NDS and mAP performance but exhibits low ASR. We attribute this to the temporal consistency enforced by its use of explicit front and rear frame inputs, which enhances robustness, consistent with observations from [23]. We compare our method with the most relevant baseline, Adv3D [17], as shown in Tab. 2.

Unlike Adv3D, which significantly degrades detection performance across the entire scene, our method maintains scene integrity when placing adversarial objects while achieving strong targeted attacks. Category-wise AP comparisons further reveal that our method is particularly effective against the vehicle class, demonstrating superior adversarial strength with minimal collateral impact.

## 4.3 Qualitative Results

Fig. 3 and Fig. 5 illustrate the effectiveness of our attack in both the 2D image and BEV views. Our method successfully suppresses or biases model predictions while introducing false positives.

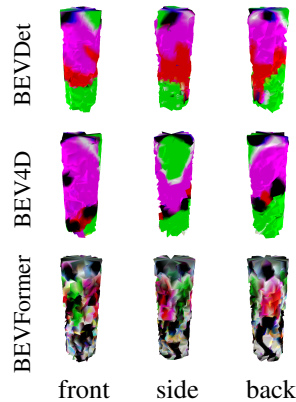


Figure 4: Visualization of adversarial objects generated for different models.

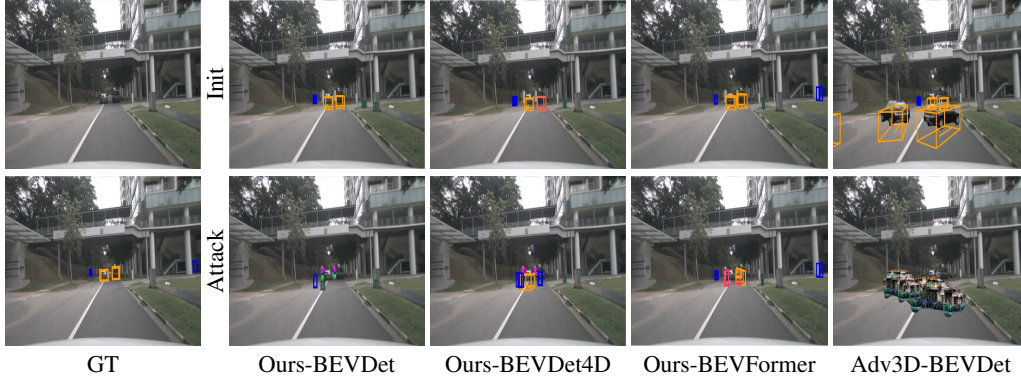


Figure 3: **Visualizations of attack effects in image view.** with comparison with Adv3D [17].

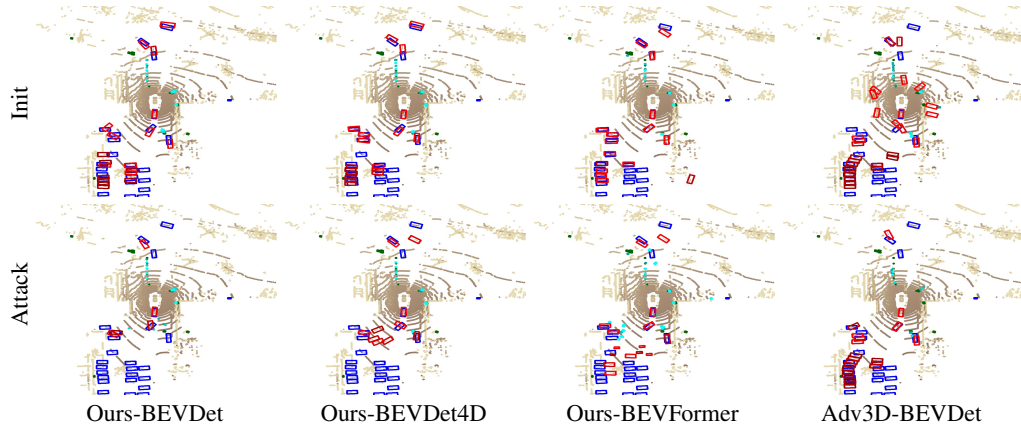


Figure 5: **Visualizations of attack effects in the BEV.** Top: predictions with initial objects. Bottom: predictions after inserting the adversarial object. Blue/red indicate ground-truth/predicted boxes for vehicles; green/cyan for other object categories.

Importantly, the 2D results demonstrate that the attack’s impact is not due to occlusion or coverage, but rather stems from exploiting the inherent vulnerability of the 3D detection model. In Fig. 4, we visualize adversarial objects optimized against different detectors. Notably, the object optimized for BEVFormer exhibits pedestrian-like textures, suggesting the model may have learned semantically incorrect associations.

#### 4.4 Ablation Study

**Initialization of 3D objects with different shapes:** We study the effect of initial mesh shape on attack performance, including cylinder, cube, and sphere. All meshes are positioned at a distance of 0.1 from the bottom-right corner of the target vehicle to avoid collision. The *cylinder* mesh contains 1642 vertices and 3240 faces, with a base radius of 0.3 and a height of 2.0. The *cube* mesh contains 726 vertices and 1200 faces, with each edge measuring 0.9 unit. The *sphere* mesh consists of 2562 vertices and 5120 faces, with a radius of 0.5. The attack performance of different shapes of mesh is shown in Tab. 3. While the cube is not significantly more effective than the sphere or cylinder in attacking the entire scene, it consistently achieves higher success rates against the broader vehicle category than sphere. As visualized in Fig. 6, we attribute this to the cube’s geometric similarity to vehicles, which facilitates the generation of adversarial textures that are more likely to be semantically associated with

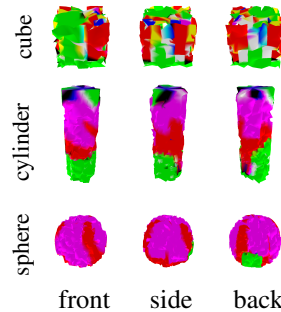


Figure 6: Visualization of adversarial objects generated for different models.

vehicles. Notably, the cylinder also performs well, likely due to its comparable height to vehicles, enabling stronger spatial interaction with model-predicted vehicle regions.

Table 3: **Attack performance comparison regarding different shape as initialization on BEVDet.**

Shape	Real Occ	Init NDS	Adv NDS	Init mAP	Adv mAP	ASR 0.3	ASR 0.5
Clean	-	0.3942	-	0.3086	-	-	-
Sphere	✗	0.3627	0.2402	0.2661	0.1534	0.565	0.614
Sphere	✓	0.3736	0.2948	0.2818	0.1958	0.310	0.367
Cube	✗	0.3473	0.2210	0.2493	0.1450	0.609	0.677
Cube	✓	0.3661	0.2882	0.2735	0.1846	0.369	0.455
Cylinder	✗	0.3579	0.2097	0.2625	0.1298	0.613	0.657
Cylinder	✓	0.3727	0.2677	0.2797	0.1631	0.447	0.510

**Attack distance:** Since the 3D adversarial object does not contact the target vehicle, we evaluate its influence at varying distances to assess the spatial range of its effect. Specifically, we train and test with the adversarial object placed at different offsets from the target. Tab. 4 reports the detection performance of the target vehicle under these settings. Results show that our proposed 3D-coherent adversarial attack remains effective across a range of distances, consistently degrading detector performance with minimal impact on the surrounding scene.

**Placement generalization:** In real-world scenarios, both the ego vehicle and surrounding vehicles are typically in motion, causing the relative position between an adversarial object and its target to change over time. To simulate this, we randomly place trained adversarial meshes at different locations in the scene to evaluate the generalizability of the attack across spatial configurations. Tab. 5 reports the attack performance under varying numbers of randomly placed meshes per image. Notably, the progressively larger ASR highlights that the adversarial objects need to interact spatially around the target vehicle, and that the attack performance improves with increasing interaction and is robust over distance.

Table 4: Performance comparison at varying distances from the target, with Real. Occ.      Table 5: Performance comparison with varying numbers of randomly placed, without Real. Occ.

Dist.	Init NDS	Adv NDS	Init mAP	Adv mAP	ASR0.3	ASR0.5
Clean	0.3942	-	0.3086	-	-	-
0.1	0.3727	0.2677	0.2797	0.1631	0.446	0.510
0.3	0.3723	0.2681	0.2809	0.1619	0.449	0.513
0.5	0.3760	0.2744	0.2845	0.1659	0.427	0.491
0.7	0.3745	0.2752	0.2838	0.1677	0.416	0.492
1.0	0.3744	0.2786	0.2828	0.1687	0.430	0.478

Num.	Init NDS	Adv NDS	Init mAP	Adv mAP	ASR0.3	ASR0.5
Clean	0.3942	-	0.3086	-	-	-
1	0.3871	0.3434	0.2999	0.2433	0.175	0.130
3	0.3737	0.2735	0.2811	0.1611	0.300	0.334
5	0.3599	0.2339	0.2631	0.1085	0.401	0.508
7	0.3432	0.1781	0.2429	0.0711	0.590	0.624
10	0.3203	0.1303	0.2147	0.0342	0.793	0.744

#### 4.5 Limitation

Our method effectively suppresses vehicle predictions in non-contact scenarios. However, introducing an initialized object into the scene can cause minor prediction shifts (see first row of Fig. 3 and  $N_{init}$  in ASR). This may stem from lighting or rendering inconsistencies between our micro-renderable setup and the real image scene. Furthermore, our method shows poor performance to suppress vehicle predictions in BEVDet4D and under random object placement, indicating limited robustness to target vehicle position changes, as a key direction for future research.

### 5 Conclusion

In this paper, we have proposed a generic 3D adversarial object optimization framework that enforces both 3D spatial and inter-frame consistency. We first leverage scene geometry to identify candidate regions for contactless attacks, then introduce a physically plausible occlusion handling module to simulate realistic occlusions and improve robustness in real-world settings. To further enhance attack effectiveness across space and time, we design a BEV spatial feature-guided optimization strategy. Our deployable setup enables non-contact adversarial objects to suppress vehicle predictions in mainstream BEV-based 3D object detection models. Experimental results reveal consistent vulnerability across detectors, highlighting critical flaws in current BEV 3D perception systems.

## References

- [1] Tai Wang, Xinge Zhu, Jiangmiao Pang, and Dahua Lin. Fcos3d: Fully convolutional one-stage monocular 3d object detection. In *IEEE ICCV*, pages 913–922, 2021. 1
- [2] Yue Wang, Vitor Campagnolo Guizilini, Tianyuan Zhang, Yilun Wang, Hang Zhao, and Justin Solomon. Detr3d: 3d object detection from multi-view images via 3d-to-2d queries. In *CoRL*, pages 180–191. PMLR, 2022. 1
- [3] Zhiqi Li, Wenhai Wang, Hongyang Li, Enze Xie, Chonghao Sima, Tong Lu, Qiao Yu, and Jifeng Dai. Bevformer: Learning bird’s-eye-view representation from lidar-camera via spatiotemporal transformers. *IEEE T-PAMI*, 47(03):2020–2036, 2025. 1
- [4] Xuyang Bai, Zeyu Hu, Xinge Zhu, Qingqiu Huang, Yilun Chen, Hongbo Fu, and Chiew-Lan Tai. Transfusion: Robust lidar-camera fusion for 3d object detection with transformers. In *IEEE CVPR*, pages 1090–1099, 2022. 1
- [5] Zhijian Liu, Haotian Tang, Alexander Amini, Xinyu Yang, Huizi Mao, Daniela L Rus, and Song Han. Bevfusion: Multi-task multi-sensor fusion with unified bird’s-eye view representation. In *IEEE ICRA*, pages 2774–2781, 2023. 1, 2
- [6] Yin hao Li, Zheng Ge, Guanyi Yu, Jinrong Yang, Zengran Wang, Yukang Shi, Jianjian Sun, and Zeming Li. Bevdepth: Acquisition of reliable depth for multi-view 3d object detection. In *AAAI*, volume 37, pages 1477–1485, 2023. 1, 2
- [7] Junjie Huang, Guan Huang, Zheng Zhu, Yun Ye, and Dalong Du. Bevdet: High-performance multi-camera 3d object detection in bird-eye-view. *arXiv preprint arXiv:2112.11790*, 2021. 1, 2, 7
- [8] Adam W Harley, Zhaoyuan Fang, Jie Li, Rares Ambrus, and Katerina Fragkiadaki. Simple-bev: What really matters for multi-sensor bev perception? In *IEEE ICRA*, pages 2759–2765, 2023. 1
- [9] Zhenxin Li, Shiyi Lan, Jose M Alvarez, and Zuxuan Wu. Bevnex: Reviving dense bev frameworks for 3d object detection. In *IEEE CVPR*, pages 20113–20123, 2024. 1
- [10] Miaoyu Li, Yachao Zhang, Xu Ma, Yanyun Qu, and Yun Fu. Bev-dg: Cross-modal learning under bird’s-eye view for domain generalization of 3d semantic segmentation. In *IEEE ICCV*, pages 11632–11642, 2023. 1
- [11] Hai Chen, Huanqian Yan, Xiao Yang, Hang Su, Shu Zhao, and Fulan Qian. Efficient adversarial attack strategy against 3d object detection in autonomous driving systems. *IEEE T-ITS*, 25(11):16118–16132, 2024. 1, 3
- [12] James Tu, Huichen Li, Xinchun Yan, Mengye Ren, Yun Chen, Ming Liang, Eilyan Bitar, Ersin Yumer, and Raquel Urtasun. Exploring adversarial robustness of multi-sensor perception systems in self driving. In *CoRL*, pages 1013–1024. PMLR, 2021. 1, 2, 3
- [13] Lu Wang, Tianyuan Zhang, Yikai Han, Muyang Fang, Ting Jin, and Jiaqi Kang. Attack end-to-end autonomous driving through module-wise noise. In *IEEE CVPR*, pages 8349–8352, 2024. 1
- [14] Man Zhou, Wenyu Zhou, Jie Huang, Junhui Yang, Minxin Du, and Qi Li. Stealthy and effective physical adversarial attacks in autonomous driving. *IEEE Trans. Inf. Forensics Secur.*, 19:6795–6809, 2024. 1
- [15] Jian Wang, Fan Li, Song Lv, Lijun He, and Chao Shen. Physically realizable adversarial creating attack against vision-based bev space 3d object detection. *IEEE T-IP*, 34:538–551, 2025. 1, 3
- [16] Jian Wang, Fan Li, and Lijun He. A unified framework for adversarial patch attacks against visual 3d object detection in autonomous driving. *IEEE T-CSVT*, 35(5):4949–4962, 2025. 1, 2, 3
- [17] Leheng Li, Qing Lian, and Ying-Cong Chen. Adv3d: Generating 3d adversarial examples for 3d object detection in driving scenarios with nerf. In *IEEE IROS*, pages 10813–10820, 2024. 1, 2, 3, 4, 7, 8

- [18] Alexander Lehner, Stefano Gasperini, Alvaro Marcos-Ramiro, Michael Schmidt, Mohammad-Ali Nikouei Mahani, Nassir Navab, Benjamin Busam, and Federico Tombari. 3d-vfield: Adversarial augmentation of point clouds for domain generalization in 3d object detection. In *IEEE CVPR*, pages 17295–17304, 2022. 1, 3
- [19] Donghua Wang, Tingsong Jiang, Jialiang Sun, Weien Zhou, Zhiqiang Gong, Xiaoya Zhang, Wen Yao, and Xiaoqian Chen. Fca: Learning a 3d full-coverage vehicle camouflage for multi-view physical adversarial attack. In *AAAI*, volume 36, pages 2414–2422, 2022. 1, 2
- [20] Jiakai Wang, Aishan Liu, Zixin Yin, Shunchang Liu, Shiyu Tang, and Xianglong Liu. Dual attention suppression attack: Generate adversarial camouflage in physical world. In *IEEE CVPR*, pages 8565–8574, 2021. 1, 2
- [21] Naufal Suryanto, Yongsu Kim, Hyoeun Kang, Harashta Tatimma Larasati, Youngyeo Yun, Thi-Thu-Huong Le, Hunmin Yang, Se-Yoon Oh, and Howon Kim. Dta: Physical camouflage attacks using differentiable transformation network. In *IEEE CVPR*, pages 15305–15314, 2022. 1, 3
- [22] Naufal Suryanto, Yongsu Kim, Harashta Tatimma Larasati, Hyoeun Kang, Thi-Thu-Huong Le, Yoonyoung Hong, Hunmin Yang, Se-Yoon Oh, and Howon Kim. Active: Towards highly transferable 3d physical camouflage for universal and robust vehicle evasion. In *IEEE ICCV*, pages 4305–4314, 2023. 1, 3
- [23] Shaoyuan Xie, Zichao Li, Zeyu Wang, and Cihang Xie. On the adversarial robustness of camera-based 3d object detection. *Trans. Mach. Learn. Res.*, 2024. 2, 3, 4, 7
- [24] Zijian Zhu, Yichi Zhang, Hai Chen, Yinpeng Dong, Shu Zhao, Wenbo Ding, Jiachen Zhong, and Shibao Zheng. Understanding the robustness of 3d object detection with bird’s-eye-view representations in autonomous driving. In *IEEE CVPR*, pages 21600–21610, 2023. 2, 3
- [25] Mazen Abdelfattah, Kaiwen Yuan, Z Jane Wang, and Rabab Ward. Towards universal physical attacks on cascaded camera-lidar 3d object detection models. In *2021 IEEE international conference on image processing (ICIP)*, pages 3592–3596. IEEE, 2021. 2
- [26] Jindi Zhang, Yang Lou, Jianping Wang, Kui Wu, Kejie Lu, and Xiaohua Jia. Evaluating adversarial attacks on driving safety in vision-based autonomous vehicles. *IEEE Internet Things J.*, 9(5):3443–3456, 2021. 2, 3
- [27] Mazen Abdelfattah, Kaiwen Yuan, Z Jane Wang, and Rabab Ward. Adversarial attacks on camera-lidar models for 3d car detection. In *IEEE IROS*, pages 2189–2194, 2021. 2, 3
- [28] Xiaohui Zeng, Chenxi Liu, Yu-Siang Wang, Weichao Qiu, Lingxi Xie, Yu-Wing Tai, Chi-Keung Tang, and Alan L Yuille. Adversarial attacks beyond the image space. In *IEEE CVPR*, pages 4302–4311, 2019. 2
- [29] Chaowei Xiao, Dawei Yang, Bo Li, Jia Deng, and Mingyan Liu. Meshadv: Adversarial meshes for visual recognition. In *IEEE CVPR*, pages 6898–6907, 2019. 2
- [30] Qiming Lu, Shikui Wei, Haoyu Chu, and Yao Zhao. Towards transferable 3d adversarial attack. In *MMAAsia*, pages 1–5, 2021. 2
- [31] Anish Athalye, Logan Engstrom, Andrew Ilyas, and Kevin Kwok. Synthesizing robust adversarial examples. In *ICML*, pages 284–293, 2018. 2
- [32] Scott Oslund, Clayton Washington, Andrew So, Tingting Chen, and Hao Ji. Multiview robust adversarial stickers for arbitrary objects in the physical world. *J. Comput. Cogn. Eng.*, 1(4):152–158, 2022. 3
- [33] Yao Huang, Yinpeng Dong, Shouwei Ruan, Xiao Yang, Hang Su, and Xingxing Wei. Towards transferable targeted 3d adversarial attack in the physical world. In *IEEE CVPR*, pages 24512–24522, 2024. 3
- [34] Tom B Brown, Dandelion Mané, Aurko Roy, Martín Abadi, and Justin Gilmer. Adversarial patch. *arXiv preprint arXiv:1712.09665*, 2017. 3

- [35] Darren Yu Yang, Jay Xiong, Xincheng Li, Xu Yan, John Raiti, Yuntao Wang, HuaQiang Wu, and Zhenyu Zhong. Building towards" invisible cloak": Robust physical adversarial attack on yolo object detector. In *IEEE UEMCON*, pages 368–374, 2018. 3
- [36] Stephen Casper, Max Nadeau, Dylan Hadfield-Menell, and Gabriel Kreiman. Robust feature-level adversaries are interpretability tools. In *NeurIPS*, volume 35, pages 33093–33106, 2022. 3
- [37] Donghua Wang, Wen Yao, Tingsong Jiang, Chao Li, and Xiaoqian Chen. Rfla: A stealthy reflected light adversarial attack in the physical world. In *IEEE ICCV*, pages 4455–4465, 2023. 3
- [38] Jian Wang, Fan Li, Xuchong Zhang, and Hongbin Sun. Adversarial obstacle generation against lidar-based 3d object detection. *IEEE T-MM*, 26:2686–2699, 2023. 3
- [39] Yifan Zhang, Junhui Hou, and Yixuan Yuan. A comprehensive study of the robustness for lidar-based 3d object detectors against adversarial attacks. *IJCV*, 132(5):1592–1624, 2024. 3
- [40] Yizhou Wang, Libing Wu, Jiong Jin, Enshu Wang, Zhuangzhuang Zhang, and Yu Zhao. An imperceptible adversarial attack against 3d object detectors in autonomous driving. *IEEE Internet Things J.*, 2025. 3, 4
- [41] James Tu, Mengye Ren, Sivabalan Manivasagam, Ming Liang, Bin Yang, Richard Du, Frank Cheng, and Raquel Urtasun. Physically realizable adversarial examples for lidar object detection. In *IEEE CVPR*, pages 13716–13725, 2020. 3
- [42] Ben Mildenhall, Pratul P Srinivasan, Matthew Tancik, Jonathan T Barron, Ravi Ramamoorthi, and Ren Ng. Nerf: Representing scenes as neural radiance fields for view synthesis. In *ECCV*, pages 405–421, 2020. 3, 4
- [43] Nikhila Ravi, Jeremy Reizenstein, David Novotny, Taylor Gordon, Wan-Yen Lo, Justin Johnson, and Georgia Gkioxari. Accelerating 3d deep learning with pytorch3d. *arXiv preprint arXiv:2007.08501*, 2020. 5
- [44] Nikhila Ravi, Valentin Gabeur, Yuan-Ting Hu, Ronghang Hu, Chaitanya Ryali, Tengyu Ma, Haitham Khedr, Roman Rädle, Chloe Rolland, Laura Gustafson, et al. Sam 2: Segment anything in images and videos. *arXiv preprint arXiv:2408.00714*, 2024. 5
- [45] Holger Caesar, Varun Bankiti, Alex H Lang, Sourabh Vora, Venice Erin Liong, Qiang Xu, Anush Krishnan, Yu Pan, Giancarlo Baldan, and Oscar Beijbom. nusenes: A multimodal dataset for autonomous driving. In *IEEE CVPR*, pages 11621–11631, 2020. 6, 7
- [46] Junjie Huang and Guan Huang. Bevdet4d: Exploit temporal cues in multi-camera 3d object detection. *arXiv preprint arXiv:2203.17054*, 2022. 7
- [47] Zhiqi Li, Wenhai Wang, Hongyang Li, Enze Xie, Chonghao Sima, Tong Lu, Qiao Yu, and Jifeng Dai. Bevformer: learning bird’s-eye-view representation from lidar-camera via spatiotemporal transformers. *IEEE T-PAMI*, 2024. 7
- [48] Benjin Zhu, Zhengkai Jiang, Xiangxin Zhou, Zeming Li, and Gang Yu. Class-balanced grouping and sampling for point cloud 3d object detection. *arXiv preprint arXiv:1908.09492*, 2019. 7

## Appendix

In the appendix, we provide further comparisons of evaluation metrics alongside visualization comparisons of our proposed **Meeseeks Mesh** in [Appendix A](#). Additionally, we supplement the transferability under black-box attack in [Appendix B](#), and more robustness analysis with respect to distance in [Appendix C](#).

### A Additional Evaluation Metrics for White-Box Attacks

Considering the varying object sizes and weights in the nuScenes dataset, where IoU is typically not used, we follow the nuScenes evaluation protocol. [Tab. 6](#) reports mean Average Precision (mAP) for the vehicle category and detection results of cars at different sensor ranges. For example,  $AP_{car0.5}$  denotes the average precision for vehicles within 0.5 meters of the sensor. The results demonstrate that our 3D adversarial samples consistently reduce vehicle detection accuracy, particularly within 0.5 meters, highlighting both the vulnerability of current BEV models and the potential for severe impact in close-range scenarios. In addition, we show more visualized comparisons in [Fig. 7](#) and [Fig. 8](#).

Table 6: Performance comparison of BEV-based 3D object detection on adversarial attack with Real. Occ.

	Init/Adv mAP <sub>vel</sub>		Init/Adv AP <sub>car0.5</sub>		Init/Adv AP <sub>car1.0</sub>		Init/Adv AP <sub>car2.0</sub>		Init/Adv AP <sub>car4.0</sub>	
BEVDet	0.210	0.076	0.1691	0.0493	0.419	0.1984	0.6304	0.3475	0.7483	0.4453
BEVDet4D	0.221	0.089	0.1762	0.0408	0.4309	0.1784	0.6476	0.3373	0.7551	0.4756
BEVFormer	0.302	0.154	0.1783	0.0824	0.4520	0.3029	0.7136	0.5381	0.8365	0.6798

### B Results of 3D Adversarial Objects under Transfer Attacks

To verify the generalization of 3D adversarial objects across models, we evaluate transfer attacks on scenarios and vehicle categories using BEVDet, BEVDet4D, and BEVFormer ([Tab. 7](#) and [Tab. 8](#)). The results demonstrate that 3D adversarial objects consistently exploit vulnerabilities shared across these BEV models, regardless of the scenario or target category.

Table 7: Performance comparison of attack on scenes by 3D adversarial objects under transfer attacks. The first row shows the victim model; the first column shows the source mesh model.

source \ victim	Init		BEVDet (Adv)		BEVDet4D (Adv)		BEVFormer (Adv)	
	NDS	mAP	NDS / mAP	NDS / mAP	NDS / mAP	NDS / mAP	NDS / mAP	
BEVDet	0.3727	0.2797	0.2677	0.1631	0.2819	0.1775	0.3125	0.2124
BEVDet4D	0.4304	0.2929	0.3573	0.2070	0.3385	0.1885	0.3633	0.2190
BEVFormer	0.4681	0.3565	0.4348	0.3112	0.4330	0.3113	0.3381	0.2073

Table 8: Performance comparison of attack on Vehicle category by 3D adversarial objects under transfer attacks. The first row shows the victim model; the first column shows the source model.

source \ victim	Init			BEVDet (Adv)			BEVDet4D (Adv)			BEVFormer (Adv)		
	mAP <sub>vel</sub>	AP <sub>car0.5</sub>	AP <sub>car2.0</sub>	mAP <sub>vel</sub>	AP <sub>car0.5</sub>	AP <sub>car2.0</sub>	mAP <sub>vel</sub>	AP <sub>car0.5</sub>	AP <sub>car2.0</sub>	mAP <sub>vel</sub>	AP <sub>car0.5</sub>	AP <sub>car2.0</sub>
BEVDet	0.210	0.1691	0.6304	0.076	0.0493	0.3475	0.092	0.0735	0.4105	0.135	0.1113	0.5398
BEVDet4D	0.221	0.1762	0.6476	0.112	0.0677	0.4161	0.089	0.0408	0.3373	0.135	0.1214	0.5562
BEVFormer	0.302	0.1783	0.7136	0.244	0.1526	0.6371	0.243	0.1515	0.6353	0.154	0.0824	0.5381

### C Distance Robustness

In **Attack distance** in [Sec. 4.4](#), we compare the results of training 3D adversarial objects at different locations. To further assess spatial robustness, we place a mesh trained at 0.5 units across varying distances ([Tab. 9](#)). The adversarial object successfully attacks the target category across all test locations, indicating robustness over distance. While the attack is most effective near the training

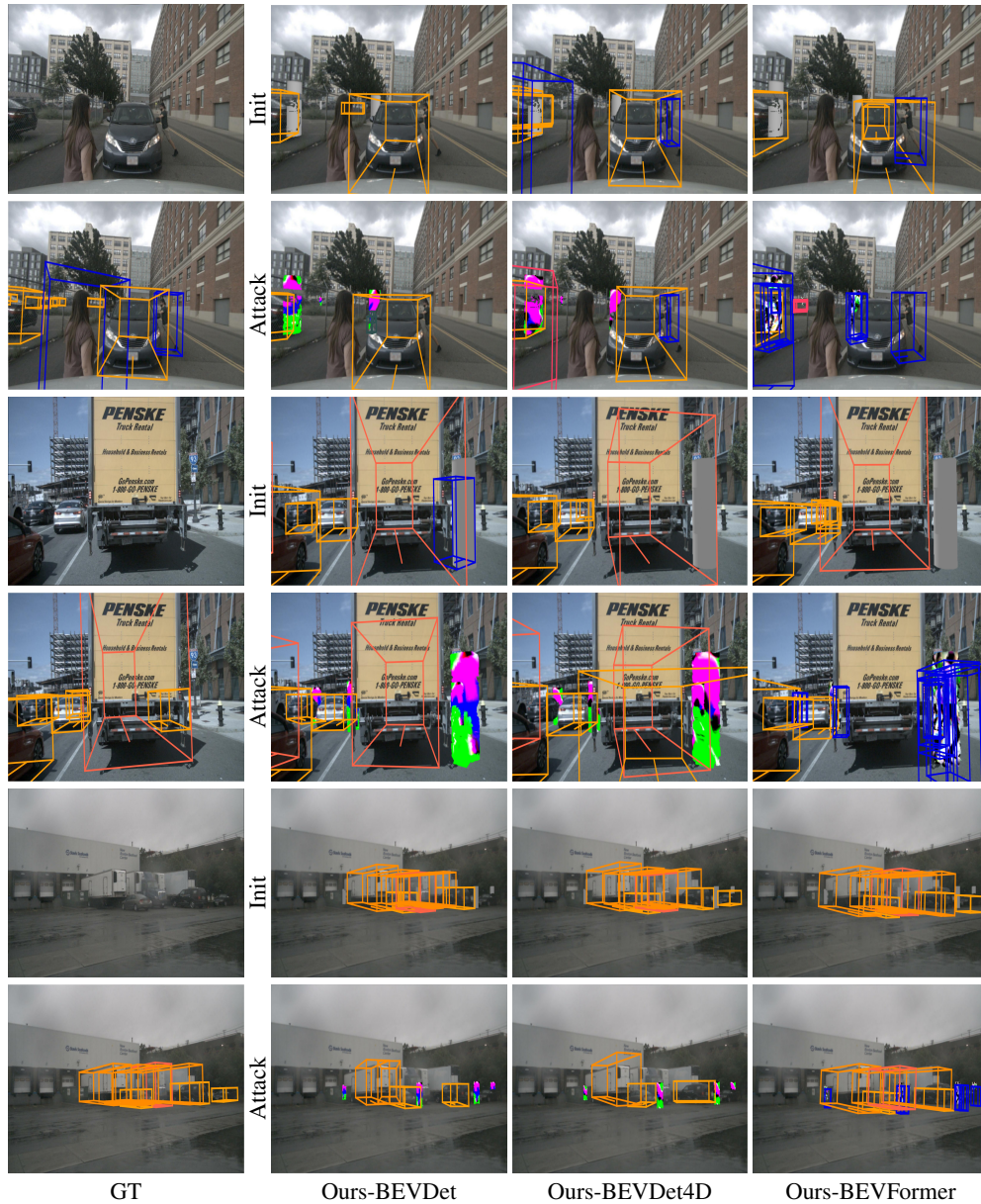


Figure 7: Visualizations of attack effects in image view.

position, ASR gradually declines as the placement moves farther away. This also explains why the ASR in the Sec.4.4 **Placement Generalization** experiment is lower when the number of meshes is small: insufficient object coverage leads to the adversarial mesh far away from the target vehicle and thus failed target attack.

Table 9: Comparison of attack performance when placing a 3D adversarial object, trained at distance=0.5, from the target vehicles at varying distances, with Real. Occ.

Distance	Init NDS	Adv NDS	Init mAP	Adv mAP	ASR 0.3	ASR 0.5
Clean	0.3942	-	0.3086	-	-	-
0.1	0.3728	0.2702	0.2796	0.1648	0.444	0.503
0.3	0.3720	0.2751	0.2808	0.1657	0.436	0.500
0.5	0.3760	0.2744	0.2845	0.1659	0.427	0.491
0.7	0.3746	0.2774	0.2838	0.1673	0.424	0.476
1.0	0.3745	0.2818	0.2827	0.1712	0.434	0.482
1.5	0.3763	0.2849	0.2845	0.1743	0.453	0.473
2.0	0.3742	0.2825	0.2818	0.1765	0.422	0.472
2.5	0.3743	0.2925	0.2843	0.1834	0.405	0.457
3.0	0.3763	0.2973	0.2880	0.1890	0.391	0.444

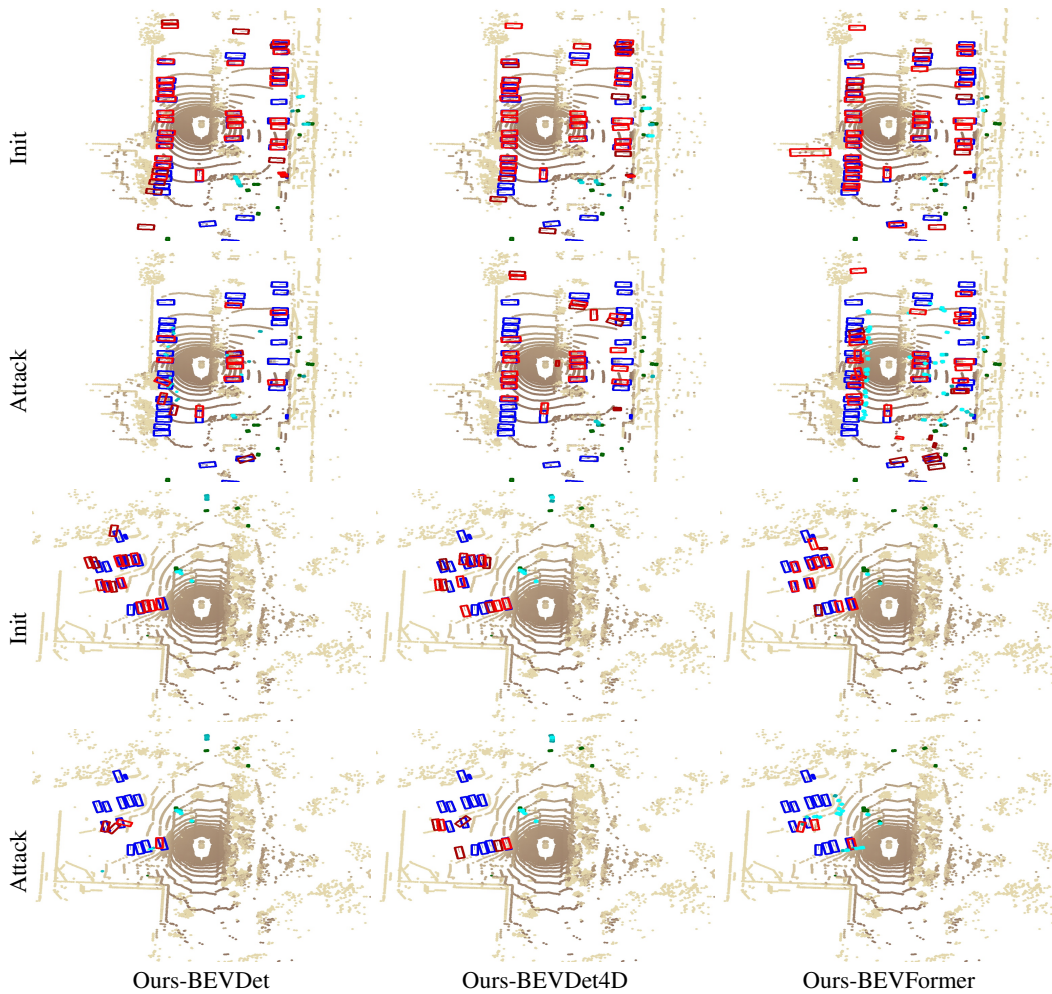


Figure 8: **Visualizations of attack effects in the BEV.** Top: predictions with initial objects. Bottom: predictions after inserting the adversarial object. Blue/red indicate ground-truth/predicted boxes for vehicles; green/cyan for other object categories.